2-14-2012

Gravity-wave-induced Variations in Exothermic Heating in the Low-latitude, Equinox Mesophere and Lower Thermosphere Region

Michael P. Hickey Ph.D.
Embry-Riddle Aeronautical University, hicke0b5@erau.edu

Tai-Yin Huang

Scholarly Commons Citation
Journal of Geophysical Research, vol. 117, A02307, doi: https://doi.org/10.1029/2011JA017148

Gravity-wave-induced variations in exothermic heating in the low-latitude, equinox mesophere and lower thermosphere region

Tai-Yin Huang[1] and Michael Hickey[2]

Received 9 September 2011; revised 16 November 2011; accepted 13 December 2011; published 14 February 2012.

[1] We investigate gravity-wave-induced variations in exothermic heating in the OH nightglow region at a latitude of 18° in the Northern and Southern Hemispheres during March. An OH nightglow chemistry model with gravity wavefields from a spectral full-wave model is used for the investigation. Our simulation results show that the wave packet induces a large secular increase in the number densities of the minor species involved in the OH chemistry, a 50% increase in O_3, 42% in O, and 29% in OH ($v = 8$), and the ultimate driver for these increases is the wave-driven downward transport of O. We find that the total exothermic heating rates have increased by ∼44.2% for 18°S and ∼30.9% for 18°N by the end of the simulation time. Also, the peak values of the mean wave-induced total exothermic heating rates are significant, ∼2.0 K d^{-1} at the peak altitude of 88 km and ∼2.2 K d^{-1} at 89 km for 18°S and 18°N, respectively. The major reactions contributing to exothermic heating rates are the three-body recombination O + O + M and the H + O_3 reaction. The hemispheric asymmetry in the heating rates is mainly due to the different atmospheric conditions at 18°N and 18°S since the same wavefields are used in the numerical simulations.

Citation: Huang, T.-Y., and M. Hickey (2012), Gravity-wave-induced variations in exothermic heating in the low-latitude, equinox mesophere and lower thermosphere region, *J. Geophys. Res.*, *117*, A02307, doi:10.1029/2011JA017148.

1. Introduction

[2] Gravity wave forcing has been an intense research topic in the field of aeronomy since 1960 when *Hines* [1960] established that gravity waves were responsible for ionospheric disturbances. Gravity waves are important because they can transport energy and momentum to higher altitudes, deposit energy and momentum through wave-mean flow interactions, alter gas concentration distributions by the combined effects of vertical transport of species and chemistry, and induce exothermic heating variations. They play an important role in the dynamics and energy budget in the mesosphere and lower thermosphere (MLT) region. It has long been recognized that gravity wave effects in the MLT region are significant. Therefore, it is important that we understand gravity waves and their effects on our atmosphere.

[3] In addition to gravity waves, the airglow in the MLT region is another important research topic in our scientific community. It is important because variations in airglow brightness can oftentimes be used to deduce characteristics of gravity waves or other types of waves that cause the variations. Observations of airglow brightness have shown that gravity waves are a ubiquitous feature in the upper atmosphere. The presence of wave-like patterns in the airglow imagery, a manifestation of wave modulation of the underlying minor species' densities involved in the airglow chemistry, arises from the coupling of wave dynamics and chemistry in that region. Gravity waves can also manifest themselves in the ionosphere as fluctuations in electron density (so-called traveling ionospheric disturbances), and in the upper mesosphere they can also lead to structure observed in noctilucent clouds. Furthermore, a transient and dissipative wave packet propagating through an airglow layer can lead to a secular change in the airglow brightness [*Hickey and Walterscheid*, 2001; *Huang and Hickey*, 2008].

[4] In recent years, airglow observations and theoretical studies have significantly advanced our understanding of gravity waves and their interactions with the airglow layers [*Walterscheid et al.*, 1987; *Hecht and Walterscheid*, 1991; *Schubert et al.*, 1991; *Taylor et al.*, 1995; *Liu and Swenson*, 2003; *Huang and Hickey*, 2008; *Taori et al.*, 2007]. In particular, a 2-D, time-dependent, OH nightglow chemistry-dynamics model developed by Huang and Hickey [*Hickey et al.*, 2003; *Huang and Hickey*, 2007, 2008] is capable of simulating the interaction of a dissipative, transient gravity wave packet with the OH nightglow layer. Importantly, some of the chemical reactions considered in the 2-D OH nightglow chemistry-dynamics model are exothermic, and thus the model also simulates how a gravity wave packet affects the exothermic heating rates in the OH nightglow region [*Hickey et al.*, 2003]. In addition to simulating wave-induced exothermic heating fluctuations [*Hickey et al.*, 2003], the model can simulate secular variations of minor species [*Huang and Hickey*, 2007] and secular variations of OH airglow brightness [*Huang and Hickey*, 2008]. These studies

[1]Department of Physics, Pennsylvania State University-Lehigh Valley, Center Valley, Pennsylvania, USA.
[2]Department of Physical Sciences, Embry-Riddle Aeronautical University, Daytona Beach, Florida, USA.

0148-0227/12/2011JA017148

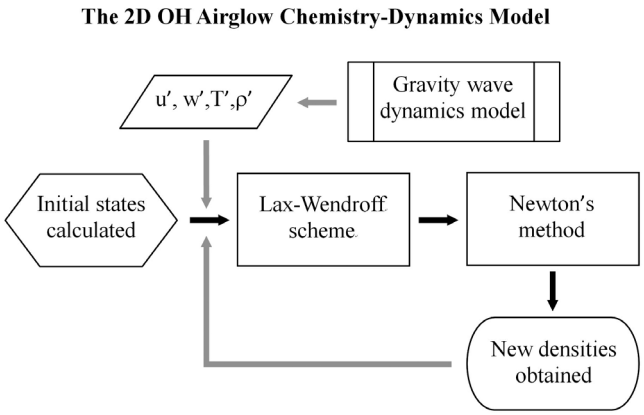

Figure 1. Schematic diagram of the 2-D OH airglow chemistry-dynamics model.

using the 2-D OH nightglow chemistry-dynamics model have shown that a transient dissipating gravity wave packet can induce a significant secular increase in the concentrations of minor species and in the OH airglow brightness. Since heating rates are proportional to the product of gas species' number densities, we can expect the wave packet to have a significant effect on the exothermic heating rates. The studies elucidate the role of a gravity wave packet in the airglow intensity variations and show that the ultimate driver for the increases is the gravity-wave-driven downward transport of O. These time-dependent studies also show rather different gravity wave effects when compared with the results from previous steady state studies.

[5] Chemical heating from exothermic chemical reactions contributes significantly to the energy budget of the MLT region [*Kellogg*, 1961; *Mlynczak and Solomon*, 1991]. It was shown that exothermic chemical reactions are the single largest heat source near the mesopause [*Mlynczak*, 1996]. Gravity waves can affect minor species' concentrations in the region, which will consequently affect the exothermic heating generated from the chemical reactions involving these species. Therefore, studying the wave effects on the exothermic heating rates is important in understanding the role gravity waves play in the thermal budget in this region. *Hickey et al.* [2003] used the aforementioned model to investigate the wave effects on exothermic heating. Their results show that a 20 min, 30 km (horizontal wavelength of the forcing wave) wave packet could induce a substantial increase in the total exothermic heating rates at a latitude of 82°N. The average wave-induced total exothermic heating rate was found to be $\sim$1.8 K d^{-1} or a $\sim$22% increase. Contrary to the previous steady state model predictions that gravity waves mitigate exothermic heating [*Hickey and Walterscheid*, 1994; *Xu et al.*, 2000], the results using the 2-D, time-dependent model indicate that the wave packet overall acts to raise the heating rates, increasing thermal energy in this region. In this study, we use the same 2-D OH chemistry-dynamics model to investigate wave-induced exothermic heating rate variations at 18°S and 18°N and we investigate in detail the respective contribution of each exothermic chemical reaction to the thermal energy budget in this region. The 18°N and 18°S regions were chosen for the simulations because there are relatively more gravity wave and OH airglow observations at low latitudes. A separate paper on airglow simulation results compared with airglow observations is planned for a future study.

[6] The paper is arranged as follows. We discuss exothermic heating reactions in section 2 and present results in section 3. Discussion and conclusions are provided in sections 4 and 5, respectively.

2. The 2-D OH Nightglow Chemistry-Dynamics Model and Exothermic Heating

[7] The 2-D, time-dependent, nonlinear OH nightglow chemistry-dynamics model consists of a spectral full-wave model (SFWM) and a 2-D, OH nightglow chemistry model. Figure 1 shows the schematic flowchart of the 2-D OH model. The SFWM [*Hickey et al.*, 2000] is used to provide a transient, dissipative, linear gravity wave packet comprising wave periods from 5 min to 40 h, and it solves for and outputs wave-perturbed quantities: u' (horizontal velocity), w' (vertical velocity), T' (temperature), and ρ' (major gas density). The wave packet is damped by eddy and molecular diffusions. The wave solution as a function of time and altitude is then input to the two-dimensional nonlinear time-dependent OH chemistry model to study the interaction of the gravity wave packet with the chemically reacting species in the OH nightglow region. Flux terms and horizontal advection terms appearing in the minor species' continuity equations are solved with the explicit finite difference Lax-Wendroff scheme [*Burstein*, 1967] while P (chemical production), L (chemical loss rate), and the vertical advection terms are solved by an implicit global Newton's method. Minor species are assumed to be in diffusive equilibrium at the upper boundary and remain constant at the lower boundary. Periodic lateral boundary conditions are applied at the lateral boundaries, which are spaced one horizontal wavelength apart. A source height at 10 km altitude above ground is specified to provide the wave forcing. A time step of 3 s is used along with a 0.1 km vertical grid and a 0.5 km lateral grid in the model. The time domain of the simulation is from 120 to 540 min.

[8] A wave packet of a 20 min forcing-wave period and a 30 km horizontal wavelength is simulated with the SFWM. The envelope of the wave packet amplitude grows with altitude until it reaches a maximum value near 105 km altitude after which it starts to decrease. Figure 2 displays the amplitude of the wave packet at 90 km altitude as a function of time. The wave packet forces the major gas species N_2 to oscillate, and at 90 km altitude the maximum amplitude is $\sim$1.2% of the N_2 number density occurring at around 320–340 min.

[9] Table 1 lists the reactions considered for the OH(8,3) nightglow chemistry, the enthalpies, the heating rates, and the heating efficiencies for the exothermic reactions. The reaction rates and the enthalpies are the same as those used by *Huang and Hickey* [2007, 2008] and *Hickey et al.* [2003], respectively. The references for these quantities can be found therein. Note that reaction R_7 in Table 1 was considered by *Hickey et al.* [2003] but not listed in their paper. In addition, the ordering of the reactions in their paper is different from the ordering in the later papers that used the same model. The $H + O_3$ reaction has a heating efficiency of 0.6 (constant with altitude) while all other reactions have unit heating efficiency

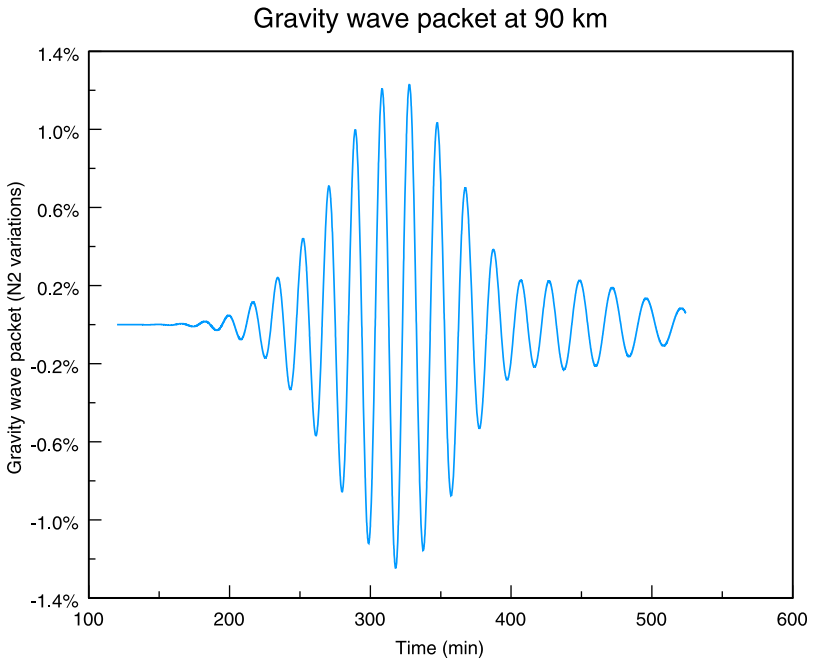

Figure 2. The gravity wave packet with a forcing-wave period of 20 min and horizontal wavelength of 30 km. It shows the wave packet amplitudes at 90 km altitude as functions of time.

[*Mlynczak and Solomon*, 1993]. *Mlynczak and Solomon* [1993, Figure 17] calculated heating efficiencies for the $H + O_3$ reaction using four different kinetic models, and the calculated values show a large uncertainty. The 0.6 value is approximately midway between the calculated highest and the lowest heating efficiency limits, and its use is recommended for it minimizes the error in the calculated heating rate.

[10] Six species are considered in the OH nightglow chemistry: O, O_3, H, HO_2, OH (v = 0), and OH* (v = 8). Initial number densities of O and H in March at 18°S and 18°N are taken from *Garcia and Solomon* [1985] and supplied by R. R. Garcia (private communication, 1990). Major gas densities of N_2 and O_2 and the temperature profiles are taken from MSIS-90 [*Hedin*, 1991]. The initial profiles for the rest of the species (O_3, HO_2, OH ($v = 0$), and OH*($v = 8$)) are calculated by assuming that they are initially in chemical balance. Therefore, the whole initial background profiles form a self-consistent system.

[11] For a chemical reaction $A + B \rightarrow C + D$, the heating rate Q is equal to $\varepsilon ER[A][B]$, where ε is heating efficiency, E is enthalpy, R is the reaction rate, and $[A]$ and $[B]$ are concentrations of reactants A and B. We can see that heating rate depends on the gas concentrations of the reactants, the enthalpy, the heating efficiency, and the reaction rate of the exothermic heating reaction. Heating rates Q_1 through Q_7 are listed in Table 1. Since gravity waves can induce variations in the gas concentrations and temperature-dependent rate coefficients, wave-induced variations in the heating rates are expected. To isolate the wave-induced variations, we first find the average values for the accumulative heating rates, and then subtract the initial wave-free heating rates from the mean values. The mathematical formulation is

$$Q_{\mathrm{AVG}} = \frac{1}{N}\sum_{i=0}^{N} Q(t_i) - Q(t_0), \tag{1}$$

Table 1. OH(8,3) Nightglow Chemistry, Enthalpies, Exothermic Heating Rates, and Heating Efficiencies

	Reaction	Enthalpy E (kcal mol^{-1})	Heating Rate Q	Heating Efficiency ε
R_1	$O + OH\ (v = 0) \rightarrow H + O_2$	$E_1 = -16.77$	$Q_1 = \varepsilon_1 * R_1 * E_1 * [O][OH]$	1
R_2	$H + O_2 + M \rightarrow HO_2 + M$	$E_2 = -49.10$	$Q_2 = \varepsilon_2 * R_2 * E_2 * [H][O_2][M]$	1
R_3	$O+HO_2 \rightarrow OH\ (v = 0) + O_2$	$E_3 = -53.27$	$Q_3 = \varepsilon_3 * R_3 * E_3 * [O][HO_2]$	1
R_4	$O + O + M \rightarrow O_2 + M$	$E_4 = -119.4$	$Q_4 = \varepsilon_4 * R_4 * E_4 * [O]^2[M]$	1
R_5	$O + O_2 + M \rightarrow O_3 + M$	$E_5 = -25.47$	$Q_5 = \varepsilon_5 * R_5 * E_5 * [O][O_2][M]$	1
R_6	$H + O_3 \rightarrow OH^*\ (v = 8) + O_2$	$E_6 = -76.90$	$Q_6 = \varepsilon_6 * (R_6 + R_7) * E_6 * [H][O_3]$	0.6
R_7	$H + O_3 \rightarrow OH\ (v = 0) + O_2$			
R_8	$OH^*\ (v = 8) \rightarrow OH\ (v = 3) + h$			
R_9	$OH^*\ (v = 8) + O \rightarrow H + O_2$	$E_7 = -16.77$	$Q_7 = \varepsilon_7 * R_9 * E_7 * [OH^*(v = 8)][O]$	1
R_{10}	$OH^*\ (v = 8) + O_2 \rightarrow OH\ (v - 1) + O_2$			
R_{11}	$OH^*\ (v = 8) + N_2 \rightarrow OH\ (v - 1) + N_2$			

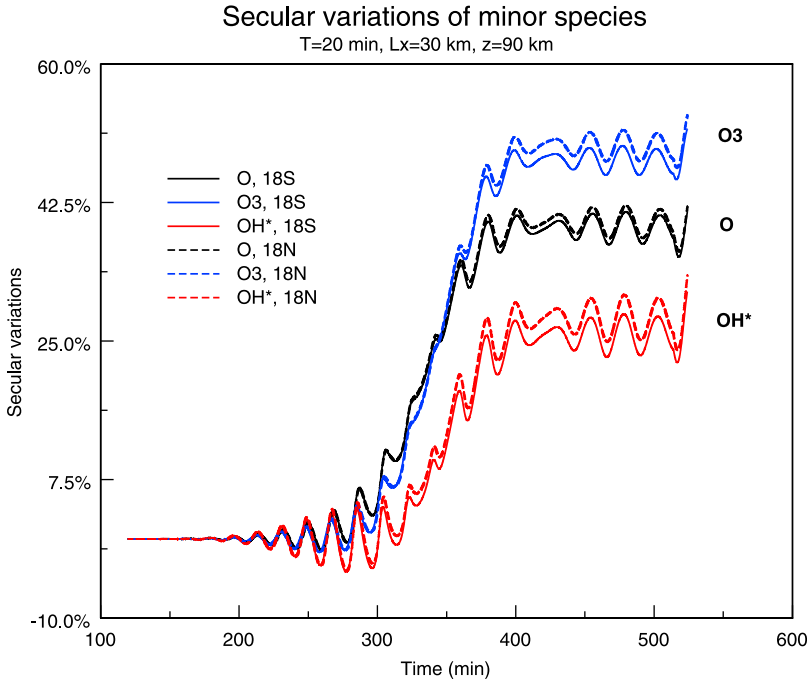

Figure 3. Secular variations of O, O_3, and OH* (v = 8) number densities at 90 km altitude at 18°S and 18°N. The solid lines are for 18°S and the dashed lines are for 18°N. Steep increases occur at ~300 min and last for ~80 min.

where Q_{AVG} is the average wave-induced heating rate and N is the number of iterations.

3. Results

[12] In this section, we present the simulation results for two latitudes (18°N and 18°S) using the same gravity wave packet with a forcing wave period of 20 min and a horizontal wavelength of 30 km. The wave source is located in the troposphere, with the resulting wave amplitude growing exponentially and reaching a maximum near 105 km altitude, beyond which the amplitude decreases because of dissipation. Since gravity waves induce variations in the gas species' number densities, we first study how the number densities vary under the influence of the wave packet. We focus on the species (O, O_3, and OH*) appearing in reactions R_4 and R_6 because these reactions have larger enthalpies than the rest.

[13] Figure 3 shows the secular variations of O, O_3, and OH* (v = 8) number densities at 90 km altitude as a function of time at 18°S (solid curves) and 18°N (dashed curves): blue for O_3, black for O, and red for OH*. The secular variations of the number densities are obtained by performing a running average, with the window size equal to the forcing-wave period T = 20 min. This procedure separates the number density variations into two parts: the fluctuating part that oscillates at the forcing-wave period and the secular part that survives this averaging [see *Huang and Hickey*, 2007]. From Figure 3, we can identify that strong secular variations occur approximately around the time when the forcing wave amplitude is about to reach the peak value. A steep increase in the secular variations starts at around 300 min and lasts for about 100 min. After that, the variations seem to reach a plateau, with smaller variations occurring until the end of the simulation time. It is interesting to note that the slopes of the number density increase are somewhat similar to the slope of the wave amplitude growth. The small oscillations seen in the secular variations are due to the fact that performing a running average at the forcing-wave period will not remove oscillations occurring at all periods comprising the wave packet. Nevertheless, aside from the small oscillations, these secular variations of the three species show a common feature: a small increase in the beginning followed by a steep increase when the wave amplitude reaches the peak value; then the variations remain comparable for the remainder of the simulation time. Of the three species, O_3 shows the largest secular increase of ~50%, followed by O (~42%), and then OH (v = 8) (~29%) at the end of the simulation. These results indicate that the gravity wave packet induces significant secular variations in the gas species' number densities. Since heating rates are proportional to the product of gas species' number densities, we can expect the wave packet to have a significant effect on the exothermic heating rates. Note that the variations at 18°S are smaller than, but similar to, those at 18°N.

[14] To understand how the gravity wave packet affects the exothermic heating rates in the OH nightglow region, we plotted the initial and the final heating rates for each exothermic reaction for 18°S in Figures 4a and 4b, respectively. These heating rates are presented in units of K d^{-1}, but it should be borne in mind that they only represent the nighttime heating rates since we consider nighttime chemistry. From inspecting Figure 4, we can see that Q_4 is the major heat contributor and peaks at a much higher altitude than the other heating rates. It has the largest enthalpy (−119.4 kcal mol^{-1}) and is proportional to the product of [M] and $[O]^2$.

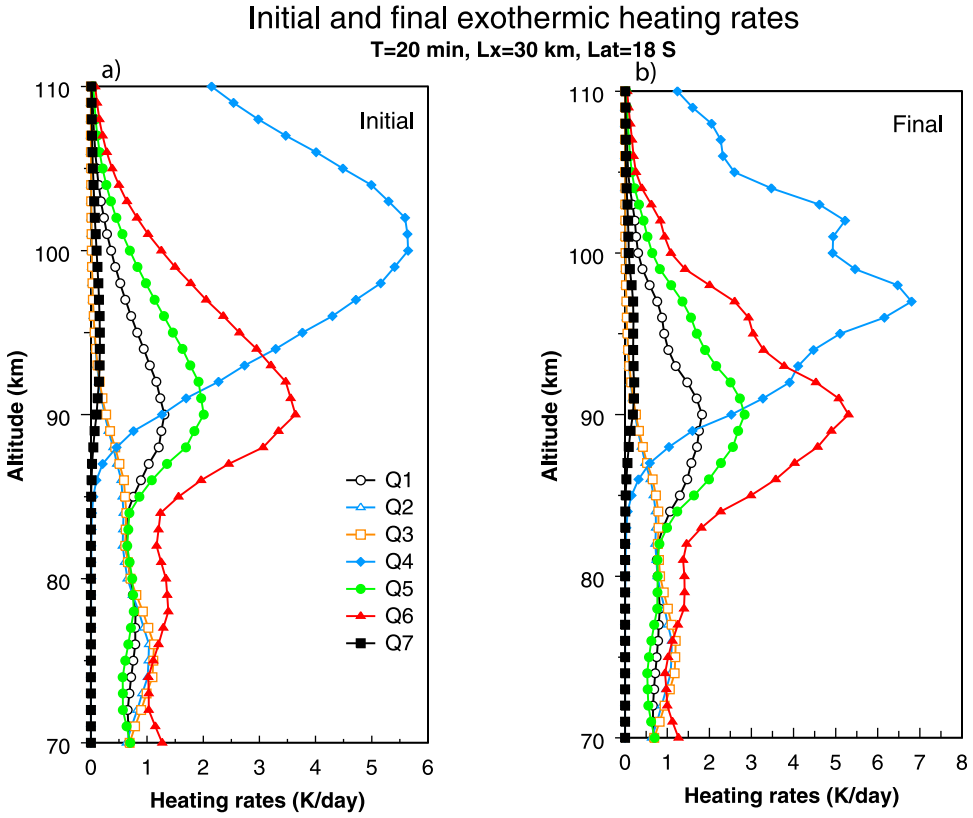

Figure 4. (a) Initial and (b) final exothermic heating rates Q_1 through Q_7 for 18°S. The black curve with open circles denotes Q_1, the blue curve with open triangles denotes Q_2, the orange curve with open squares denotes Q_3, the blue curve with solid diamonds denotes Q_4, the green curve with solid circles denotes Q_5, the red curve with solid triangles denotes Q_6, and, finally, the black curve with solid squares denotes Q_7. Q_4 and Q_6 are the major heating rates. The initial heating rate Q_4 peaks at 101 km altitude with a peak value of 5.64 K d^{-1} while the final Q_4 peaks at 97 km with a value of 6.8 K d^{-1}.

The initial peak height for Q_4 is located at 101 km altitude with a peak value of 5.64 K d^{-1}, while the final peak height for Q_4 is located near 97 km altitude with a peak value of 6.8 K d^{-1}. At a time of 420 min the wave activity has caused Q_4 to increase by 1.16 K d^{-1} (∼21%) and the peak altitude to be displaced downward by 4 km. It is not surprising that Q_4 peaks at a relatively high altitude because it is proportional to the square of the atomic oxygen number density. Previous studies have shown that the gravity wave packet can induce a significant downward flux of O [*Hickey and Walterscheid*, 2001; *Huang and Hickey*, 2007, 2008]. The lower peak height of the Q_4 final heating rate is largely due to the downward transport of O.

[15] The second major heat contributor is Q_6, with the peak altitude remaining at the same height of 90 km for the initial and the final heating rates. Q_6 has the second largest enthalpy (−76.9 kcal mol^{-1}) and is proportional to the product of [H] and [O_3]. The initial peak value is 3.64 K d^{-1}, and the final peak value is 5.08 K d^{-1}, representing a ∼40% increase. The third major heat contributor is Q_5, with an initial peak height at 90 km altitude and a peak value of 2.01 K d^{-1}. The final peak height remains at 90 km altitude, and the peak value is increased to 2.84 K d^{-1} (∼41% increase). As for Q_1, the initial peak value is 1.31 K d^{-1} and the final peak value is 1.83 K d^{-1} (∼40% increase) while the peak height also remains at 90 km altitude. The rest of the heating rates (the initial and the final values) are either close to or less than 1 K d^{-1}.

[16] We plotted the initial and the final exothermic heating rates for each exothermic reaction for 18°N in Figures 5a and 5b, respectively. Figure 5 shows features very similar to those shown in Figure 4 but with larger heating rates. Q_4 remains the largest heating rate followed by Q_6, then Q_5. The peak altitude for Q_4 lies a few kilometers above the peak altitudes for the rest of the heating rates. The initial peak altitude for Q_4 is at 100 km, and the final peak altitude is at 97 km at the end of the simulation. The peak value changes from 7.38 to 8.83 K d^{-1}, representing an ∼20% heating rate increase. Q_6 initially peaks at 92 km altitude with a value of 4.8 K d^{-1}; then it moves down to 91 km with a value of 6.79 K d^{-1}, indicating a ∼42% heating rate increase. The initial and final peak altitudes for Q_5 are the same as those for Q_6. The initial peak value for Q_5 is 2.65 K d^{-1}, and the final peak value is 3.63 K d^{-1}, showing a 37% increase in the heating rate. The initial and the final peak values for Q_1 are 1.64 and 2.31 K d^{-1}, respectively, and it represents a ∼41% increase.

[17] The previous two figures show the individual heating rates. Next we show the initial and final total heating rates at 18°S in Figure 6a and at 18°N in Figure 6b. The black solid curve denotes the initial total heating rate, and the red dashed curve denotes the final total heating rate. From Figure 6 and

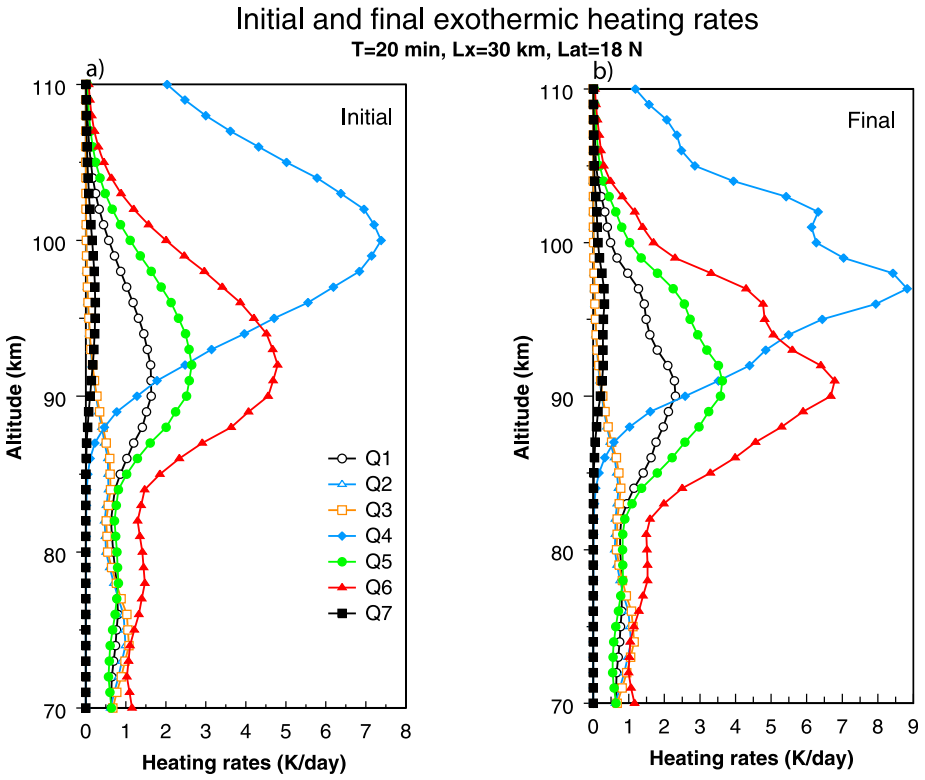

Figure 5. (a) Initial and (b) final exothermic heating rates Q_1 through Q_7 for 18°N. Again, Q_4 and Q_6 are the major heating rates. The initial heating rate Q_4 peaks at 100 km altitude with a peak value of 7.38 K d^{-1} while the final Q_4 peaks at 97 km with a value of 8.83 K d^{-1}.

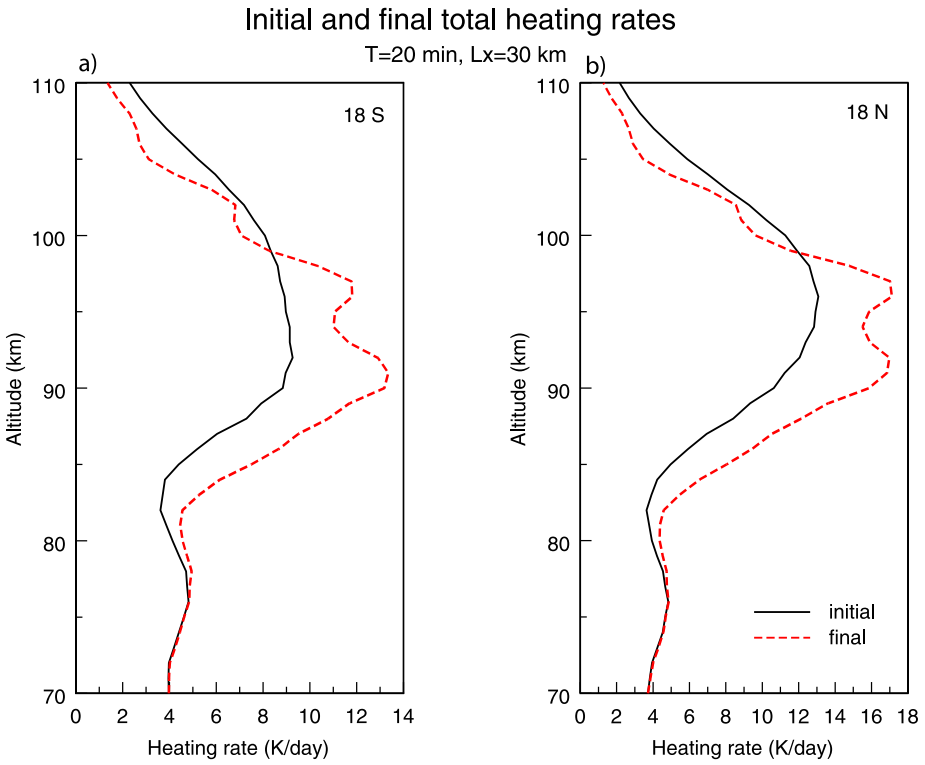

Figure 6. Initial and final total heating rates Q_{total} for (a) 18°S and (b) 18°N. The total heating rates at 18°N are larger than those at 18°S. The wave-like structure is apparent in the final heating rates.

Table 2. Initial and Final Peak Values (K d^{-1}) and Peak Altitudes (km) at 18°S

	Q_i	Q_f	Percent	Z_i	Z_f	ΔZ
Q_1	1.31	1.83	39.7	90	90	–
Q_2	1.04	1.11	6.7	76	76	–
Q_3	1.12	1.2	7.1	76	76	–
Q_4	5.64	6.8	20.6	101	97	−4
Q_5	2.01	2.84	41.3	90	90	–
Q_6	3.64	5.08	39.6	90	90	–
Q_7	0.16	0.22	37.5	94–95	92	$-2 \sim -3$
Q_{total}	9.26	13.35	44.2	92	91	−1

Figures 4b and 5b, we can see wave-like structures in the final total heating rates at both latitudes. This is expected since these data are not the running average values and so they retain the wave signatures. The initial total heating rates display a single prominent peak at both latitudes while the final total heating rates display a double-peak-like feature that is due to the presence of the wave packet. The initial total heating rate at 18°S peaks at 92 km with a value of 9.26 K d^{-1}, and the final total heating rate peaks at 91 km with a value of 13.35 K d^{-1}. The initial total heating rate at 18°N peaks at a higher altitude at 96 km with a value of 13.08 K d^{-1}, while the final total heating rate peaks at two locations, ~96 and 92 km, with roughly the same value of 17.12 K d^{-1}. Comparing the peak values of the initial and final heating rates, we see that the heating rates are increased by 4.09 K d^{-1} (~44%) at 18°S and 4.04 K d^{-1} (~31%) at 18°N by the end of the simulation. We note that the overall final total heating rates increase between 77 and 99 km and decrease above 99 km altitude when they are compared with the initial heating rate values for both latitudes. The percent change of Q_{total} at 18°S is larger than that at 18°N mainly because the Q_{total} changes are roughly the same for 18°S and 18°N but the initial value of Q_{total} at 18°N is considerably greater than that at 18°S. The peak altitudes and magnitudes of the initial and final heating rates at 18°S and 18°N are tabulated in Tables 2 and 3, respectively. We also include in the tables the heating rate percent changes and the altitude changes for easier inspection.

[18] Figures 4–6 show a direct comparison of the final heating rate values to the initial heating rate values. To find the average wave-induced variations in the exothermic heating rates, we use equation (1). Figures 7 and 8 show the vertical profiles of mean wave-induced heating rate variations for Q_1 through Q_{total} at 18°S and 18°N, respectively. The largest mean wave-induced total exothermic heating rate Q_{total} is 1.98 K d^{-1} at 88 km altitude at 18°S and 2.19 K d^{-1} at 89 km altitude at 18°N. Comparing these mean wave-induced heating rates with the initial heating rates at the same altitude shows that the wave packet can induce a mean 28.3% (24.4%) increase in the total exothermic heating rate at 18°S (at 18°N). The gravity wave packet induces larger heating rates in Q_4 and Q_6 followed by Q_5 and Q_1 for both latitudes. The peak value of the mean wave-induced heating rate for Q_4 is 0.81 (1.06) K d^{-1} and for Q_6 is 0.88 (0.95) K d^{-1} at 18°S (18°N). The peak values and the peak altitudes of the mean wave-induced heating rates are listed in Table 4. Figures 7 and 8 also show that the overall effects of the gravity wave packet are to increase exothermic heating rates below 100 km (99 km) altitude for 18°S (18°N) and to decrease exothermic heating rates above that altitude. The largest decrease occurs at 105 km (104 km) altitude at 18°S (18°N) with a value of −0.69 K d^{-1} (−0.87 K d^{-1}), and the single largest decrease comes from the contribution of reaction R_4, the three-body recombination. This result is not surprising since it is consistent with the depletion of atomic O at higher altitudes (e.g., downward flux of O to lower altitudes) and Q_4 is proportional to $[O]^2$. These results show that the gravity wave packet not only modulates the distribution of gas concentrations but also causes rather significant variations in the heating rates and alters the vertical distribution of the heating region.

4. Discussion

[19] *Hecht et al.* [1995] reported an observation that showed a steep increase in OH airglow intensity without an appreciable increase in OH temperature. They suggested that the intensity enhancement might be caused by a nonperiodic change in atmospheric composition, specifically, a rapid wave-induced downward flux of ozone in the airglow layer. Our simulations of OH nightglow intensity and the intensity-weighted temperature in the presence of a gravity wave packet (not shown) display a steep increase in the nightglow intensity without a noticeable change in the temperature. Our simulation results are very similar to what Hecht et al. observed. Our Figure 3 shows a steep increase in the O_3, O, and OH* number densities, which seems to support the suggested mechanism by Hecht et al. The studies by *Hickey and Walterscheid* [2001] and *Huang and Hickey* [2007, 2008] have shown that it is the wave-induced downward flux of O in the airglow region that increases the atomic oxygen number density in the reactions that produce O_3 and OH* and that eventually leads to a steep increase in the airglow intensity. Their studies elucidate the role of the gravity wave packet in the airglow intensity variations and show that the ultimate driver for the increases is the gravity-wave-driven downward transport of O. The O_3 increase is a consequence of the combination of the enhanced O number density in chemical reactions and wave dynamics. Their studies also indicate that the onset of the airglow intensity increase occurs after the wave packet has passed the maximum amplitude by a few wave cycles. One of the results discussed by *Huang and Hickey* [2008] is that background diffusion and chemistry (the initial tendency) tends to cause a steep decline in OH nightglow intensity [see *Huang and Hickey*, 2008, Figure 7] until a steady state is reached. When an upward propagating gravity wave is present, the wave acts to increase the airglow intensity. *Huang and Hickey* [2008, Figure 4] shows the simulation result of the wave packet competing

Table 3. Initial and Final Peak Values (K d^{-1}) and Peak Altitudes (km) at 18°N

	Q_i	Q_f	Percent	Z_i	Z_f	ΔZ
Q_1	1.64	2.31	40.9	90	90	–
Q_2	0.99	1.06	7.1	74	74	–
Q_3	1.08	1.15	6.5	74	74	–
Q_4	7.38	8.83	19.6	100	97	−3
Q_5	2.65	3.63	37	92	91	−1
Q_6	4.8	6.79	41.5	92	91	−1
Q_7	0.24	0.31	29.2	96	96	–
Q_{total}	13.08	17.12	30.9	96	96	–

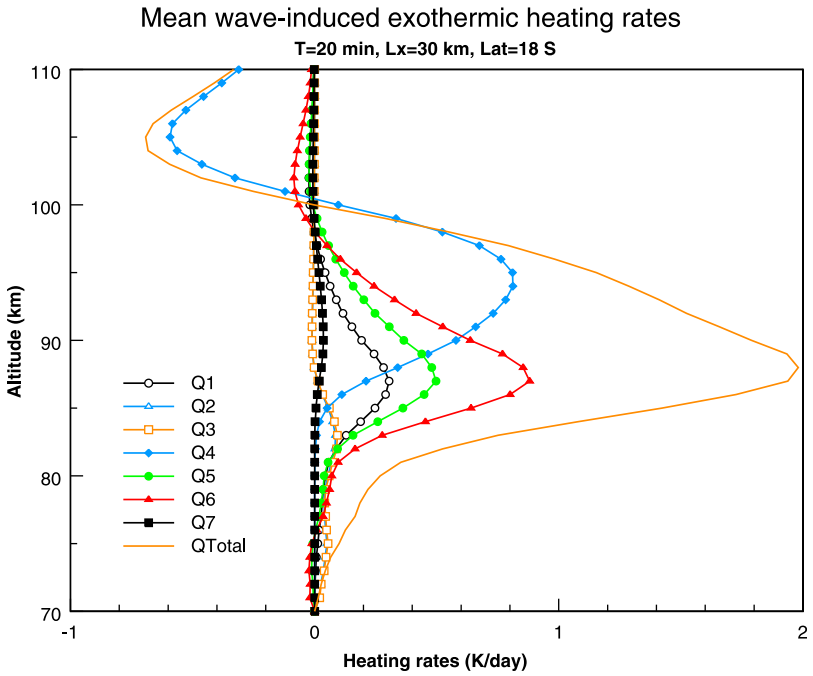

Figure 7. The mean wave-induced exothermic heating rates for 18°S. The black curve with open circles denotes Q_1, the blue curve with open triangles denotes Q_2, the orange curve with open squares denotes Q_3, the blue curve with solid diamonds denotes Q_4, the green curve with solid circles denotes Q_5, the red curve with solid triangles denotes Q_6, the black curve with solid squares denotes Q_7, and the orange solid curve denotes Q_{total}. The mean wave-induced total heating rate peaks at 88 km with a value of 1.98 K d^{-1}.

against the initial tendency. Their result seems to support the hypothesis that the steep declines in OH nightglow intensity are associated with weak gravity wave activity [*Hecht and Walterscheid*, 1991]. Not only that, their result is not in disagreement with the findings by *Hostetler and Gardner* [1994] since gravity waves have to be large enough to overcome the declines caused by the initial tendency. The observed steep increases or declines in the airglow intensity

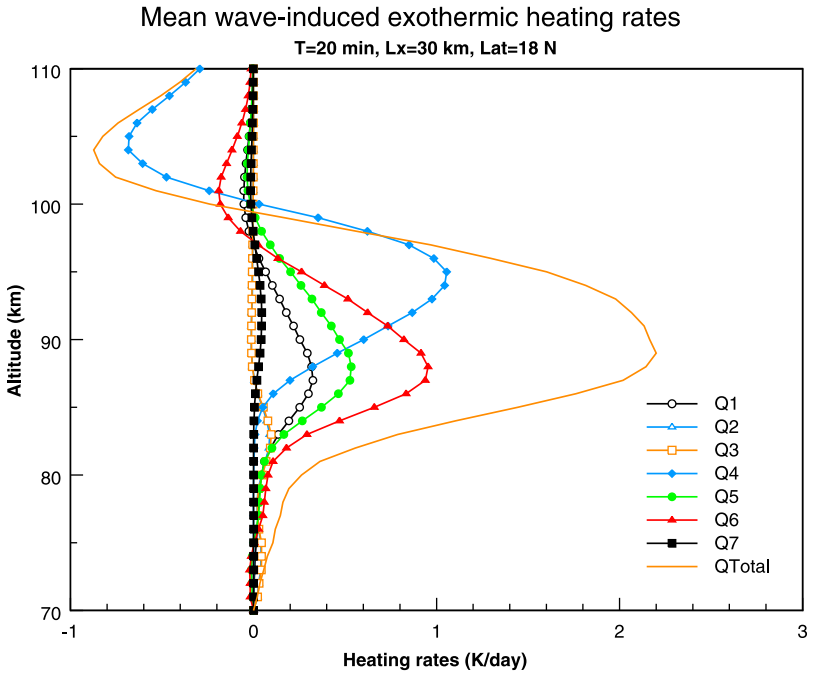

Figure 8. As in Figure 7 except for 18°N. The mean wave-induced total heating rate peaks at 89 km with a value of 2.19 K d^{-1}.

Table 4. The Peak Values (K d^{-1}) and the Peak Altitudes (km) of the Mean Wave-Induced Heating Rates at 18°S and 18°N

	18°S		18°N	
	Q_{avg}	Z_{peak}	Q_{avg}	Z_{peak}
Q_1	0.30	87	0.32	87
Q_2	0.08	83	0.08	83
Q_3	0.09	83	0.09	83
Q_4	0.81	94	1.05	95
Q_5	0.49	87	0.53	88
Q_6	0.88	87	0.95	88
Q_7	0.03	90	0.04	92
Q_{total}	1.98	88	2.19	89

and other observed features can be quite accurately simulated by our 2-D nonlinear, time-dependent OH nightglow chemistry-dynamics model.

[20] From Table 1, we can see that the OH nightglow chemiluminescence is determined in part by the number density of OH* (v = 8) in reaction R_8. A larger number density of OH* (v = 8) leads to a larger OH nightglow intensity if it radiates faster than it reacts with O or other species. Although OH*(v = 8) also contributes to heating, e.g., Q_7 from reaction R_9, we can see from Figures 4 and 5 that heating from Q_7 is very small (less than 2% of the total heating). If other higher vibrational modes were considered, the combined number densities of the OH in higher vibrational modes would be larger (reaction R_6), which would lead to more OH* (v > 0) available for chemiluminescence through reaction R_8 and fewer OH* to react with O to generate heat. Nevertheless, as mentioned above, the heat contribution from Q_7 is not significant. Our model considers one single vibrational mode, v = 8. Some might argue that our calculated heating rates might be an overestimate since other OH vibrational modes were not considered. As discussed by *Mlynczak and Solomon* [1993], there is a large uncertainty in the heating efficiency associated with the H + O_3 reaction, and one of the uncertainties comes from not knowing the exact nascent distribution of exothermicity within the OH vibrational modes. Given the large uncertainty in the heating efficiency, a 0.6 is recommended for the H + O_3 reaction. In our model, we used the recommended heating efficiency, and hence our simulation results can be deemed reasonable.

[21] The initial and final exothermic heating rates and the mean wave-induced exothermic heating rates at 18°S and 18°N were presented. It is found that the wave packet has similar effects on the exothermic heating rates at both latitudes. Since the model uses the same wave packet for both latitudes, the only difference comes from the different initial profiles of gas species and temperatures (figures not shown). The initial profiles of N_2 and O_2 at 18°N are larger than those at 18°S while the initial temperature profiles in the region of interest show that the temperature at 18°N is smaller above 89 km and larger below that altitude than the temperature at 18°S. The larger major gas species concentrations combined with the temperature structure at 18°N gives rise to higher heating rates.

[22] We compare our current results with the earlier results of a 30 km wave packet at 82°N found by *Hickey et al.* [2003]. Since the only different inputs in both studies are the initial basic states, it is found that they share similar features. The initial H + O_3 heating rate peaks at 92 km altitude with a value of ~3.5 K d^{-1} at 82°N, whereas at 18°N it peaks at the same altitude but with a larger value 4.8 K d^{-1}, and it peaks at 90 km altitude with a value of 3.64 K d^{-1} at 18°S. The final H + O_3 heating rate at 82°N peaks at ~91 km altitude with a value of 4.8 K d^{-1}. Our results show that it peaks at 91 km altitude with a value of 6.79 K d^{-1} at 18°N and at 90 km altitude with a value of 5.08 K d^{-1} at 18°S. Their initial total exothermic heating rate peaks at ~94 km altitude with a value of ~10.4 K d^{-1}, and their final total exothermic heating rate peaks at ~91 km with a value of ~13.8 K d^{-1}. Comparing these numbers with our results listed in Table 2 (for 18°S) and Table 3 (for 18°N), it is found that their initial total heating rate at 82°N is smaller than our value at 18°N (13.08 K d^{-1}) and slightly larger than the value at 18°S (9.26 K d^{-1}). The final total heating rate shows that the value at 18°N (17.12 K d^{-1}) is the largest, followed by the value at 82°N (13.8 K d^{-1}), and last by the value at 18°S (13.35 K d^{-1}). The initial peak altitude occurs at a higher altitude of 96 km at 18°N followed by 94 km altitude at 82°N and then 92 km altitude at 18°S. The final peak altitude is displaced downward by 3 km at 82°N, and by 1 km at 18 S, while no change occurs at 18°N. The peak value of the mean wave-induced heating rate is 1.8 K d^{-1} located ~90 km altitude at 82°N. Our study shows that it is 1.98 K d^{-1} at 88 km altitude at 18°S and 2.19 K d^{-1} at 89 km altitude at 18°N. These comparisons seem to suggest that the H + O_3 heating rate, the total heating rate, and the mean wave-induced heating rate at 82°N are closer to those at 18°S, while the peak altitudes of the heating rates at 82°N lie somewhat in between the peak altitudes occurring at 18°N and 18°S.

[23] Previous steady state studies of gravity wave effects on exothermic heating rates show that gravity waves act to mitigate heating [*Hickey and Walterscheid*, 1994; *Xu et al.*, 2000]. However, a recent study using a time-dependent, nonlinear OH chemistry-dynamics model shows that a dissipative, transient gravity wave packet can in fact induce a mean heating in the OH nightglow region and a mean cooling above the nightglow region [*Hickey et al.*, 2003]. Their study was for a latitude of 82°N, and they focused on the mean wave-induced heating rates. We focus our study on the respective contribution of each exothermic reaction at lower latitudes and on the mean wave-induced variations in each heating rate. Our study also shows similar features: The wave packet induces enhanced chemical exothermic heating in the OH airglow region and diminishes chemical exothermic heating above it. Further, our study indicates that the major heat contributor is the three-body recombination followed by the H + O_3 reaction. These two reactions are also the two leading cooling reactions above ~100 km.

[24] *Mlynczak and Solomon* [1991] calculated the H + O_3 heating rates and showed them in contour plots. *Mlynczak and Solomon* [1991, Figure 1] show the results using the collisional quenching rates taken from the sudden-death model of *McDade and Llewellyn* [1987], and their Figure 2 shows the results using the collisional quenching rates taken from the single-quantum-step model of *Lopez-Moreno et al.* [1987]. From inspection of the contour plots of *Mlynczak and Solomon* [1991], the H + O_3 heating rates are around 2.5 to 5 K d^{-1} at 18°S and 2 to 4 K d^{-1} at 18°N. Comparing those numbers with our initial H + O_3 heating rates (Q_6 in Tables 2 and 3) shows that our values at 18°S (3.64 K d^{-1}) and at 18°N (4.8 K d^{-1}) are similar to their values. We use

our initial values to compare with their calculations since their calculations did not include dynamics and thus were based solely on chemistry. Exothermic heating rates, using an extended set of exothermic reactions assuming no chemiluminescent loss and no dynamics, were calculated by *Mlynczak and Solomon* [1993]. The first seven exothermic heating reactions appearing in the work by *Mlynczak and Solomon* [1993, Table 4] were identified to make the most significant contributions to the total heating rates. *Mlynczak and Solomon* [1993, Figure 12] show the nighttime heating rates, obtained by summing the heating rates of the first seven reactions, to be ~8–9 K d^{-1} at 18°N and ~ 13 K d^{-1} at 18°S. Again, since they did not include dynamics in their calculations, we use our initial values for comparison. We obtain values of ~13 K d^{-1} at 18°N and ~9 K d^{-1} at 18°S. We note that their value at 18°N is similar to our value at 18°S, and vice versa. The differences might result from the different chemical reactions considered in each study. We did not include the $O + O_3$ reaction in our study. However, as pointed out by *Mlynczak and Solomon* [1993], the $O + O_3$ reaction is only a minor source of heat in the lower thermosphere. Our model included four additional reactions to allow for radiation loss and quenching by O, O_2, and N_2, which was not considered by *Mlynczak and Solomon* [1993].

[25] In addition to causing irreversible changes in the chemical exothermic heating, gravity waves also cause irreversible dynamical heating that is directly due to the divergence of the wave-driven sensible heat flux [*Walterscheid*, 1981]. *Hickey and Walterscheid* [1994] compared the wave-driven exothermic heating with the dynamical heating and found that the latter exceeded the former by a factor of ~20 near 85 km altitude for a 1 h, 140 m s^{-1} wave. We have calculated the dynamical heating for our 20 min, 25 m s^{-1} wave (not shown) and compared it with the wave-driven exothermic heating at an altitude of 90 km (which is the approximate height of maximum wave effects on the exothermic heating). We find that the dynamical heating rate is ~0.05 K d^{-1}, which is significantly smaller than the wave-driven exothermic heating rate of ~2.2 K d^{-1} (see Figure 8) at this height. However, the dynamical heating continues to grow with increasing altitude, reaching values of ~1.5 and 11 K d^{-1} at altitudes of 100 and 105 km, respectively, which exceeds the wave-driven exothermic heating rates at these altitudes. Note that the wave we are studying is much slower than the wave of *Hickey and Walterscheid* [1994], and the earlier study used a steady state model to evaluate the wave effects on the chemical exothermic heating while we have used a time-dependent model. Hence a direct comparison between these two model results should be made with caution.

5. Conclusions

[26] We investigate gravity wave effects on exothermic heating rates at 18°S and 18°N with a 2-D, time-dependent, nonlinear OH nightglow chemistry-dynamics model. Our simulation results show that the wave packet can induce the largest secular increase of ~50% in O_3, followed by O (~42%) and then OH (v = 8) (~29%) at the end of the simulation. These results indicate that significant secular variations in the gas species' number densities can be induced by a passage of a transient, dissipative gravity wave packet. With the large secular variations in the number densities, it is expected that there are large heating rate variations induced by the wave packet since the heating rates are proportional to the product of gas species' number densities. The wave-induced downward flux of O in the airglow region plays a significant role in the secular increases in the number densities and hence the heating rates. The increase of O in the airglow region increases the atomic oxygen number density in the reactions that produce O_3 and OH*, which eventually leads to a steep increase in the airglow intensity. The O_3 increase is a consequence of the combination of the enhanced O number density in chemical reactions and wave dynamics. These results elucidate the role of the gravity wave packet in the airglow intensity variations and show that the ultimate driver for the increases is the gravity-wave-driven downward transport of O. The largest heating of the exothermic chemical reactions is from the three-body recombination O + O + M, and the second largest is from the $H + O_3$ reaction. Exothermic heating is the single largest heat source in the OH nightglow region and with a dissipative gravity wave packet propagating through that region exothermic heating can be increased significantly. Further, the heating region can be altered and displaced downward. Our simulation results show that the wave packet overall acts to increase heating in the OH airglow region and to decrease the heating above the region. The peak values and peak altitudes of the total mean wave-induced exothermic heating rates are 1.98 K d^{-1} (28.3%) at 88 km for 18°S and 2.19 K d^{-1} (24.4%) at 89 km for 18°N, respectively. Our simulation results show that gravity waves not only alter the vertical distribution of gas species' concentrations through combined effect of wave transport and chemistry but also induce significant variations in the exothermic heating rates in the MLT region.

[27] **Acknowledgments.** T.-Y. Huang acknowledges support from U.S. NSF grant AGS-0836920 to The Pennsylvania State University. M. P. Hickey was supported by the National Science Foundation under grant ATM-0639293.

[28] Robert Lysak thanks the reviewers for their assistance in evaluating this paper.

References

Burstein, S. Z. (1967), Finite-difference calculations for hydrodynamic flows containing discontinuities, *J. Comput. Phys.*, *2*, 198–222, doi:10.1016/0021-9991(66)90003-9.

Garcia, R. R., and S. Solomon (1985), The effect of breaking gravity waves on the dynamics and chemical composition of mesosphere and lower thermosphere, *J. Geophys. Res.*, *90*, 3850–3868, doi:10.1029/JD090iD02p03850.

Hecht, J. H., and R. L. Walterscheid (1991), Observations of the OH Meinel (6,2) and O_2 atmospheric (0,1) Nightglow emissions from Maui during the ALOHA-90 campaign, *Geophys. Res. Lett.*, *18*, 1341–1344, doi:10.1029/91GL01152.

Hecht, J. H., S. K. Ramsay-Howat, R. L. Walterscheid, and J. R. Isler (1995), Observations of variations in airglow emissions during ALOHA-93, *Geophys. Res. Lett.*, *22*, 2817–2820, doi:10.1029/95GL03019.

Hedin, A. E. (1991), Extension of the MSIS thermosphere model into the middle and lower thermosphere, *J. Geophys. Res.*, *96*, 1159–1172, doi:10.1029/90JA02125.

Hickey, M. P., and R. L. Walterscheid (1994), Wave-modified mean exothermic heating in the mesopause region, *Geophys. Res. Lett.*, *21*, 2413–2416, doi:10.1029/94GL02504.

Hickey, M. P., and R. L. Walterscheid (2001), Secular variations of OI 5577 Å airglow in the mesopause region induced by transient gravity wave packets, *Geophys. Res. Lett.*, *28*, 701–704, doi:10.1029/2000GL012099.

Hickey, M. P., R. L. Walterscheid, and P. G. Richards (2000), Secular variations of atomic oxygen in the mesopause region induced by transient

gravity wave packets, *Geophys. Res. Lett.*, *27*, 3599–3602, doi:10.1029/2000GL011953.

Hickey, M. P., T.-Y. Huang, and R. Walterscheid (2003), Gravity wave packet effects on chemical exothermic heating in the mesopause region, *J. Geophys. Res.*, *108*(A12), 1448, doi:10.1029/2002JA009363.

Hines, C. O. (1960), Internal atmospheric gravity waves at ionospheric heights, *Can. J. Phys.*, *38*, 1441–1481, doi:10.1139/p60-150.

Hostetler, C. A., and C. S. Gardner (1994), Observations of horizontal and vertical wave number spectra of gravity wave motions in the stratosphere and mesosphere over the mid-Pacific, *J. Geophys. Res.*, *99*, 1283–1302, doi:10.1029/93JD02927.

Huang, T.-Y., and M. P. Hickey (2007), On the latitudinal variations of the non-periodic response of minor species induced by a dissipative gravity-wave packet in the MLT region, *J. Atmos. Sol. Terr. Phys.*, *69*, 741–757, doi:10.1016/j.jastp.2007.01.011.

Huang, T.-Y., and M. P. Hickey (2008), Secular variations of OH nightglow emission and of the OH intensity-weighted temperature induced by gravity-wave forcing in the MLT region, *Adv. Space Res.*, *41*, 1478–1487, doi:10.1016/j.asr.2007.10.020.

Kellogg, W. W. (1961), Chemical heating above the polar mesopause in winter, *J. Meteorol.*, *18*, 373–381, doi:10.1175/1520-0469(1961)018<0373:CHATPM>2.0.CO;2.

Liu, A. Z., and G. R. Swenson (2003), A modeling study of O_2 and OH airglow perturbations induced by atmospheric gravity waves, *J. Geophys. Res.*, *108*(D4), 4151, doi:10.1029/2002JD002474.

Lopez-Moreno, J. J., R. Rodrigo, F. Moreno, M. Lopez-Puertas, and A. Molina (1987), Altitude distribution of vibrationally excited states of atmospheric hydroxyl at levels $v = 2$ to $v = 7$, *Planet. Space Sci.*, *35*, 1029–1038, doi:10.1016/0032-0633(87)90007-9.

McDade, I. C., and E. J. Llewellyn (1987), Kinetic parameters related to sources and sinks of vibrationally excited OH in the nightglow, *J. Geophys. Res.*, *92*, 7643–7650, doi:10.1029/JA092iA07p07643.

Mlynczak, M. G. (1996), Energetics of the middle atmosphere: Theory and observation requirements, *Adv. Space Res.*, *17*(11), 117–126, doi:10.1016/0273-1177(95)00739-2.

Mlynczak, M. G., and S. Solomon (1991), Middle atmosphere heating by exothermic chemical reactions involving odd-hydrogen species, *Geophys. Res. Lett.*, *18*, 37–40, doi:10.1029/90GL02672.

Mlynczak, M. G., and S. Solomon (1993), A detailed evaluation of the heating efficiency in the middle atmosphere, *J. Geophys. Res.*, *98*, 10,517–10,541, doi:10.1029/93JD00315.

Schubert, G., R. L. Walterscheid, and M. P. Hickey (1991), Gravity wave-driven fluctuations in OH nightglow from an extended, dissipative emission region, *J. Geophys. Res.*, *96*, 13,869–13,880, doi:10.1029/91JA00562.

Taori, A., A. Guharay, and M. J. Taylor (2007), On the use of simultaneous measurements of OH and O_2 emissions to investigate wave growth and dissipation, *Ann. Geophys.*, *25*, 639–643, doi:10.5194/angeo-25-639-2007.

Taylor, M. J., M. B. Bishop, and V. Taylor (1995), All-sky measurements of short period waves imaged in the OI(557.7 nm), Na(589.2 nm) and near infrared OH and O_2(0,1) nightglow emissions during the ALOHA-93 campaign, *Geophys. Res. Lett.*, *22*, 2833–2836, doi:10.1029/95GL02946.

Walterscheid, R. L. (1981), Dynamical cooling induced by dissipating internal gravity waves, *Geophys. Res. Lett.*, *8*, 1235–1238, doi:10.1029/GL008i012p01235.

Walterscheid, R. L., G. Schubert, and J. M. Straus (1987), A dynamical-chemical model of wave-driven fluctuations in the OH nightglow, *J. Geophys. Res.*, *92*, 1241–1254, doi:10.1029/JA092iA02p01241.

Xu, J., Y. Wang, and Y. Wang (2000), The loss of photochemical heating caused by gravity waves in the mesopause region, *J. Atmos. Sol. Terr. Phys.*, *62*, 37–45, doi:10.1016/S1364-6826(99)00091-7.

M. Hickey, Department of Physical Sciences, Embry-Riddle Aeronautical University, 600 S. Clyde Morris Blvd., Daytona Beach, FL 32114, USA.

T.-Y. Huang, Department of Physics, Pennsylvania State University-Lehigh Valley, 2809 E. Saucon Valley Rd., Center Valley, PA 18034, USA. (tuh4@psu.edu)